

# Impulsively Generated Kink Wave Trains in Solar Coronal Slabs

Mingzhe Guo,<sup>1\*</sup> Bo Li,<sup>1</sup> Tom Van Doorselaere,<sup>2</sup> Mijie Shi<sup>1</sup>

<sup>1</sup>*Shandong Provincial Key Laboratory of Optical Astronomy and Solar-Terrestrial Environment, Institute of Space Sciences, Shandong University, Weihai 264209, China*

<sup>2</sup>*Centre for mathematical Plasma Astrophysics, Department of Mathematics, KU Leuven, 3001 Leuven, Belgium*

Accepted XXX. Received YYY; in original form ZZZ

## ABSTRACT

We numerically follow the response of density-enhanced slabs to impulsive, localized, transverse velocity perturbations by working in the framework of ideal magnetohydrodynamics (MHD). Both linear and nonlinear regimes are addressed. Kink wave trains are seen to develop along the examined slabs, sharing the characteristics that more oscillatory patterns emerge with time and that the apparent wavelength increases with distance at a given instant. Two features nonetheless arise due to nonlinearity, one being a density cavity close to the exciter and the other being the appearance of shocks both outside and inside the nominal slab. These features may be relevant for understanding the interaction between magnetic structures and such explosive events as coronal mass ejections. Our numerical findings on kink wave trains in solar coronal slabs are discussed in connection with typical measurements of streamer waves.

**Key words:** Magnetohydrodynamics (MHD) - Sun: corona - Sun: magnetic fields - waves

## 1 INTRODUCTION

A variety of wave events has been reported in different magnetic structures in the solar atmosphere (see Nakariakov & Kolotkov 2020, for a recent review). By swaying the axis of waveguides, kink waves tend to be readily identifiable in imaging observations and therefore have been abundantly documented (e.g., Aschwanden et al. 1999; Nakariakov et al. 1999; Tian et al. 2012; Wang et al. 2012; Anfinogentov et al. 2013; also the most recent review by Nakariakov et al. 2021). Sausage waves are usually reported in the lower portions of the solar atmosphere (e.g., Morton et al. 2012; Gao et al. 2021, and references therein), with their identification also available in coronal loops (Tian et al. 2016). Meanwhile, rapid quasi-periodic pulsations (QPPs) with periods of seconds to a couple of tens of seconds are usually attributed to fast sausage modes (see e.g., Li et al. 2020; Zimovets et al. 2021, for recent reviews). Though not easy to measure, Alfvén waves have also been reported in both spectroscopic (e.g., Jess et al. 2009) and imaging observations (e.g., Kohutova et al. 2020).

Classical modelling of waves/oscillations in the solar atmosphere usually considers a cylindrical or a slab equilibrium. Theoretical studies of collective waves in magnetic cylinders in the solar context date back to the 1970s and 1980s (e.g., Rosenberg 1970; Zaitsev & Stepanov 1975; Wentzel 1979; Spruit 1982; Edwin & Roberts 1983), and have been gaining new momentum since the first imaging observations of kink motions in coronal loops by TRACE (Aschwanden et al. 1999; Nakariakov et al. 1999). As a consequence, collective waves have been extensively examined as a possible mechanism for heating the solar corona (e.g., Howson et al. 2017; Karampelas et al. 2017; Guo et al. 2019; Shi et al. 2021; see Arregui 2015 and Van Doorselaere et al. 2020 for recent reviews). Likewise, they have been

placed in the context of coronal seismology whereby coronal parameters can be indirectly inferred (e.g., Nakariakov & Ofman 2001; Van Doorselaere et al. 2008; Guo et al. 2016; Magyar & Nakariakov 2020; see also the recent reviews by De Moortel & Nakariakov 2012 and Nakariakov & Kolotkov 2020). Waves in magnetic slabs have also been extensively investigated (e.g., Zaitsev & Stepanov 1982; Edwin & Roberts 1982; Murawski & Roberts 1993a,b; Lopin & Nagorny 2015; Yu et al. 2021). Though simple, modelling considering a slab equilibrium is intuitively associated with some coronal measurements. Two well-known typical observations are related. One is the sunward propagating waves, namely the "tadpoles" in open magnetic structures during a flare event (Verwichte et al. 2005). The other is the cyclic transverse displacements of streamer stalks, namely streamer waves, which are believed to be the largest transverse motions in the heliosphere (Chen et al. 2010, 2011; Feng et al. 2011; Kwon et al. 2013; Decraemer et al. 2020).

Impulsively excited fast magnetoacoustic wave trains are relevant for interpreting a considerable number of propagating disturbances observed in the corona. For instance, the quasi-periodic fast propagating (QFP) disturbances measured in EUV (e.g., Liu et al. 2011; Liu & Ofman 2014) can be intuitively understood as such. These fast wave trains are observed in various wavelength bands in the corona (Williams et al. 2001; Li et al. 2020, and references therein). They are examined analytically by Roberts et al. (1984) and Oliver et al. (2015), and numerically by e.g., Nakariakov et al. (2004); Yu et al. (2017); Kolotkov et al. (2021). As demonstrated in e.g., Roberts et al. (1984), the temporal signature of axisymmetric wave trains consists of distinct phases when observed sufficiently far from the exciter. These properties are attributed to the dispersive properties of fast sausage modes and are manifested in the wavelet spectrum as "crazy tadpoles" (Nakariakov et al. 2004) or "boomerangs" (Kolotkov et al. 2021). In addition, dispersive properties of impulsively generated fast kink wave trains have also been examined in coronal cylinders by e.g.,

\* E-mail: m.guo@sdu.edu.cn

Oliver et al. (2015); Yu et al. (2017). Kink wave trains in coronal holes, which are modelled as coronal funnels, are also investigated by Pascoe et al. (2014).

Until now, most studies associated with fast wave trains either focus on axisymmetric waves and their seismological potentials or discuss kink waves in magnetic cylinders. Although studies of fast kink wave trains in a zero- $\beta$  slab have been conducted by e.g., Murawski & Roberts (1993a,b); Kolotkov et al. (2021), an examination of the finite plasma  $\beta$  effect is still necessary since it may introduce slow mode modulation, as manifested in the discussion on sausage waves by Pascoe et al. (2017). In addition, it seems too ideal to consider such interactions with magnetic structures to be linear, given that the excitors of fast wave trains tend to be associated with such fierce solar activities as flares and coronal mass ejections (CMEs). However, the effect of nonlinearity has not been considered in studies associated with kink wave trains in slab configurations.

In this study, we examine the reaction of coronal slabs to impulsive, localized, transverse velocity perturbations, considering both a  $\beta = 0$  and a finite- $\beta$  effect. Meanwhile, we examine both linear and nonlinear regimes. Section 2 describes the zero- $\beta$  computation and the numerical results. Section 3 presents linear and nonlinear analyses in finite- $\beta$  MHD. Possible applications to streamer waves are discussed in Section 4. The conclusions are given in Section 5.

## 2 LINEAR COMPUTATION IN ZERO- $\beta$ MHD

In this section, we consider a coronal slab model under the cold plasma assumption ( $\beta = 0$ ) to obtain some basic understanding. We adopt linear, pressureless, ideal MHD, assuming a static equilibrium ( $v_0 = 0$ ). Working in a Cartesian coordinate system  $(x, y, z)$ , we take the equilibrium magnetic field  $\mathbf{B}_0$  to be uniform and  $z$ -directed. We further assume that the equilibrium density ( $\rho_0$ ) depends only on  $x$  and takes a step profile,

$$\rho_0(x) = \begin{cases} \rho_i, & |x| \leq d, \\ \rho_e, & |x| > d, \end{cases} \quad (1)$$

where  $d$  is the slab half-width. We define the Alfvén speed  $v_A(x)$  as  $B_0/\sqrt{\mu_0\rho_0(x)}$  with  $\mu_0$  being the magnetic permeability in free space. By  $v_{Ai}$  and  $v_{Ae}$  we refer to the values of  $v_A$  evaluated with  $\rho_i$  and  $\rho_e$ , respectively ( $v_{Ae}^2/v_{Ai}^2 = \rho_i/\rho_e$ ). For in-plane propagation ( $\partial/\partial y \equiv 0$ ), the governing equations are well known to reduce to (e.g., Terradas et al. 2005; Li et al. 2018),

$$\frac{\partial^2 \xi}{\partial t^2} = v_A^2(x) \left( \frac{\partial^2}{\partial z^2} + \frac{\partial^2}{\partial x^2} \right) \xi, \quad (2)$$

where  $\xi(x, z; t)$  is the transverse displacement. The following initial conditions (ICs) are adopted,

$$\xi(x, z; t = 0) = 0, \quad (3)$$

$$\frac{\partial \xi}{\partial t}(x, z; t = 0) = v_0 \exp\left(-\frac{x^2}{2\sigma_x^2}\right) \exp\left(-\frac{z^2}{2\sigma_z^2}\right), \quad (4)$$

where  $v_0$  represents the magnitude of the initial velocity perturbation, and  $\sigma_x$  ( $\sigma_z$ ) characterizes its spatial extent in the  $x$ - ( $z$ -) direction. We follow the evolution of an open system by adopting a uniform grid to discretize a domain that is large enough to make boundary conditions irrelevant. Initiated with the ICs, Equation (2) is advanced with a finite-difference scheme second-order accurate in both time and space (see Yu et al. 2016; Li et al. 2022, for details). We make sure that neither grid spacing nor time step affects our numerical results. The wave behavior is determined by the set  $[\rho_i/\rho_e, \sigma_x/d, \sigma_z/d]$ ,

which is fixed at  $[3, 1/\sqrt{2}, 1/\sqrt{2}]$ . The magnitude  $v_0$  is chosen such that the maximum displacement along the slab axis is  $\approx 2.6 d$ .

### 2.1 Dispersion Properties of Trapped Kink Modes

We start with an examination on the dispersion properties of kink modes by working with the well-known dispersion relation (DR; e.g., Edwin & Roberts 1982)

$$\sqrt{k^2 - \frac{\omega^2}{v_{Ae}^2}} = \sqrt{\frac{\omega^2}{v_{Ai}^2} - k^2} \tan\left(d \sqrt{\frac{\omega^2}{v_{Ai}^2} - k^2}\right), \quad (5)$$

where the angular frequency  $\omega$  and axial wavenumber  $k$  characterize a Fourier component. Focusing on trapped modes ( $\omega^2 < k^2 v_{Ae}^2$ ), we numerically solve Equation (5) for given combinations of  $[\rho_i/\rho_e, kd]$ , thereby computing the axial phase ( $v_{ph} \equiv \omega/k$ ) and group speeds ( $v_{gr} \equiv d\omega/dk$ ).

Figure 1 presents, for  $\rho_i/\rho_e = 3$ , the  $k$ -dependencies of (a)  $v_{ph}$  and (b)  $v_{gr}$ . Equation (5) admits infinitely many branches of solutions, which we label with the transverse harmonic number  $l = 1, 2, \dots$ . Figure 1 shows only the transverse fundamental ( $l = 1$ , the solid curves) and its first overtone ( $l = 2$ , dashed). Examining the fundamental, one sees that trapped modes are allowed regardless of  $k$ . In addition, both  $v_{ph}$  and  $v_{gr}$  start with  $v_{Ae}$  at  $kd \rightarrow 0$  and eventually approach  $v_{Ai}$  when  $kd \rightarrow \infty$ . However,  $v_{ph}$  does so by decreasing monotonically with  $kd$ , whereas  $v_{gr}$  first decreases with  $kd$  to some minimum (the red dot in Figure 1b) before approaching  $v_{Ai}$  from below. Moving on to the first overtone, one sees that trapped modes are permitted only when  $k$  exceeds a cutoff axial wavenumber  $k_{cutoff,2}$ . For  $k > k_{cutoff,2}$ , however, a monotonic (non-monotonic)  $k$ -dependence is seen for  $v_{ph}$  ( $v_{gr}$ ) as happens for the transverse fundamental. While only the  $l = 2$  branch is shown, all branches of trapped modes with  $l \geq 2$  are subject to cutoffs ( $k_{cutoff,l}$ ), which themselves form a monotonically increasing sequence ( $0 = k_{cutoff,1} < k_{cutoff,2} < k_{cutoff,3} < \dots$ ). In addition, the  $v_{gr} - k$  curve for each  $l$  can be divided into two portions, which will be labeled “ $l^-$ ” (“ $l^+$ ”) when  $v_{gr}$  monotonically decreases (increases) with  $k$  (see Figure 1b).

We place Figure 1 in the framework for understanding impulsively excited kink wave trains offered by Oliver et al. (2014). While developed for a cylindrical equilibrium, the Oliver et al. (2014) framework applies here because the following mathematical properties are geometry-independent<sup>1</sup>. The solutions to the eigenvalue problem pertinent to Equation (2) on an open system are distinguished by the sign of  $k_c^2 \equiv k^2 - \omega^2/v_{Ae}^2$ , with proper (improper) eigenmodes corresponding to  $k_c^2 < 0$  ( $k_c^2 > 0$ ). What we called “trapped” modes are therefore “proper” eigenmodes and will be referred to as such. The solution to our initial value problem can be formally expressed by the Fourier integral over  $k$  of individual components  $\hat{\xi}(x, k; t)$ . The  $z$ -dependence of an initial perturbation is relevant for determining  $\hat{\xi}(x, k; t = 0)$ . The  $x$ -dependence, on the other hand, determines how  $\hat{\xi}(x, k; t = 0)$  is apportioned to proper and improper eigenmodes, whose eigenfunctions depend on the equilibrium. An individual  $\hat{\xi}(x, k; t)$  at a given  $k$  therefore involves two sets of contributions. The proper set consists of  $L$  proper modes with  $L$  being such that  $k_{cutoff,L} < k < k_{cutoff,L+1}$ . The improper set collects the

<sup>1</sup> The same physics applies also to sausage-type wave trains in both cylindrical (e.g., Oliver et al. 2015; Yu et al. 2016; also Roberts et al. 1983) and Cartesian equilibria (e.g., Nakariakov et al. 2004; Pascoe et al. 2013; Kolotkov et al. 2021).

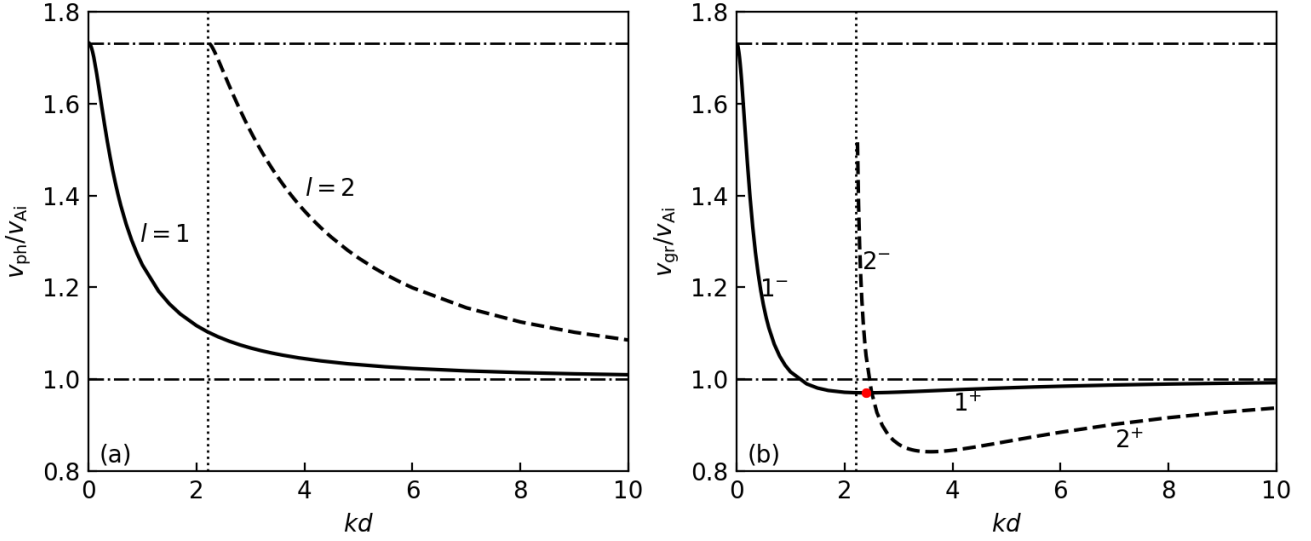


**Figure 1.** Dependence on the dimensionless wavenumber ( $kd$ ) of (a) the phase and (b) group speeds ( $v_{\text{ph}}$  and  $v_{\text{gr}}$ ) of trapped (proper) kink eigenmodes in a pressureless slab with a density contrast  $\rho_i/\rho_e = 3$ . The transverse fundamental ( $l = 1$ ) and its first overtone ( $l = 2$ ) are shown by the solid and dashed curves, respectively. The horizontal dash-dotted lines represent the internal and external Alfvén speeds ( $v_{\text{Ai}}$  and  $v_{\text{Ae}}$ ). Each curve in Figure 1b is decomposed into two portions where  $v_{\text{gr}}$  varies monotonically with  $k$ , with the red dot separating the relevant portions for  $l = 1$ .

contributions from improper modes with  $|\omega|$  extending continuously from  $kv_{\text{Ae}}$  to infinity.

The signals sampled in the slab sufficiently far from the exciter involve only the proper contributions because improper modes propagate laterally. Consider the slab axis ( $x = 0$ ). Our time-dependent results can be further placed in the framework detailed by Chapter 11 in Whitham (1974), if we focus on those  $[z, t]$  where  $z$  and  $t$  are large enough to ensure the applicability of the method of stationary phase (MSP). Seeing  $[z, t]$  as given, the so-called “stationary points” in the MSP refer to the value(s) of  $k$  that solves

$$v_{\text{gr}}(k) = \frac{z}{t}. \quad (6)$$

If  $[z, t]$  is seen as variable instead, then each solution to Equation (6) defines a local axial wavenumber  $k(z, t)$  as a function of  $z$  and  $t$ . It then makes sense to define a local phase speed  $v_{\text{ph}}(z, t)$  with the DR by seeing  $k$  therein as  $k(z, t)$ . By construction, the local group speed  $v_{\text{gr}}(z, t)$  is simply  $z/t$ . It further makes sense to define a local frequency  $\omega(z, t) = k(z, t)v_{\text{ph}}(z, t)$  and hence a local phase

$$\theta(z, t) = k(z, t)z - \omega(z, t)t. \quad (7)$$

That the MSP applies at some  $[z, t]$  means that it applies to the corresponding local phase. For brevity, we refer to such phases or space-time points as “fully developed”. We will visualize the notion that a phase needs to propagate for some time/distance to become fully developed, an intuitive expectation that has not been quantified to our knowledge. Nonetheless, the following notions apply to those fully developed phases or  $[z, t]$ . Firstly, the local values of  $k(z, t)$  and  $\omega(z, t)$  are varying (fixed) as seen by an observer moving with the local phase (group) speed. Secondly, a combination  $[k(z, t), \omega(z, t)]$  defines one wavepacket, a concept that Edwin & Roberts (1986) introduced to the solar context. Thirdly, for the problem at hand, Figure 1 indicates that a unique stationary point and hence a unique wavepacket can be determined from Equation (6) at a given  $[z, t]$  only along a monotonic portion of the  $v_{\text{gr}}(k) - k$  curve for an  $l$ .

## 2.2 Numerical Results

Figure 2 presents the  $z$ -distributions of the transverse displacement ( $\xi$ ) along the slab axis ( $x = 0$ ) at various times as labeled. Two properties can be observed from this figure. One reads that more extrema appear as time proceeds. The other is that the apparent wavelength tends to increase with distance in the snapshots of the transverse displacement. This second signature is seismologically more useful since it cannot be taken for granted but arises when some constraints are placed on, say, how the equilibrium is formulated and/or how localized the initial perturbations are. Let crest 1 and trough 1 label the outermost crest and its trailing trough (see, e.g., the red triangles at  $t = 40 d/v_{\text{Ai}}$ ). With these two local phases as examples, we illustrate that fully developed phases are bound to possess the second property if they involve only the wavepackets along the  $1^-$  portion in Figure 1b. Provided this assertion, a unique wavepacket is guaranteed for a given phase in a given instantaneous profile. Now that crest 1 leads trough 1, the instantaneous wavepacket at crest 1 necessarily possesses a larger group speed. One then deduces that the wavepacket at crest 1 necessarily possesses a smaller local wavenumber and hence a longer local wavelength, given the  $k$ -dependence of  $v_{\text{gr}}$ . Turning this argument around, one further deduces that a sufficient condition for Figure 2 to reproduce the second property for crest 1 and trough 1 is that these local phases are fully developed and the relevant wavepackets derive solely from the  $1^-$  portion.

Two questions ensue. One, how to quantify when/where a local phase is fully developed? Two, how can we assert that only portion  $1^-$  is relevant? We will address question one shortly. Accept for now that crest 1 and trough 1 are fully developed in the curves at  $t = 40 d/v_{\text{Ai}}$  and  $80 d/v_{\text{Ai}}$  because they become so when propagating beyond  $\sim 20 d$  and  $\sim 30 d$ , respectively. Take the  $t = 40 d/v_{\text{Ai}}$  curve for instance. One sees that the instantaneous group speeds ( $z/t$ ) at both phases exceed  $v_{\text{Ai}}$ , meaning that only portion  $2^-$  may be potentially relevant in addition to  $1^-$  (see Figure 1b). Assuming that portion  $2^-$  is relevant, one expects that crest 1 and/or trough 1 should be accompanied by a series of short-scale ripples because the wavepackets arriving at these locations necessarily possess large

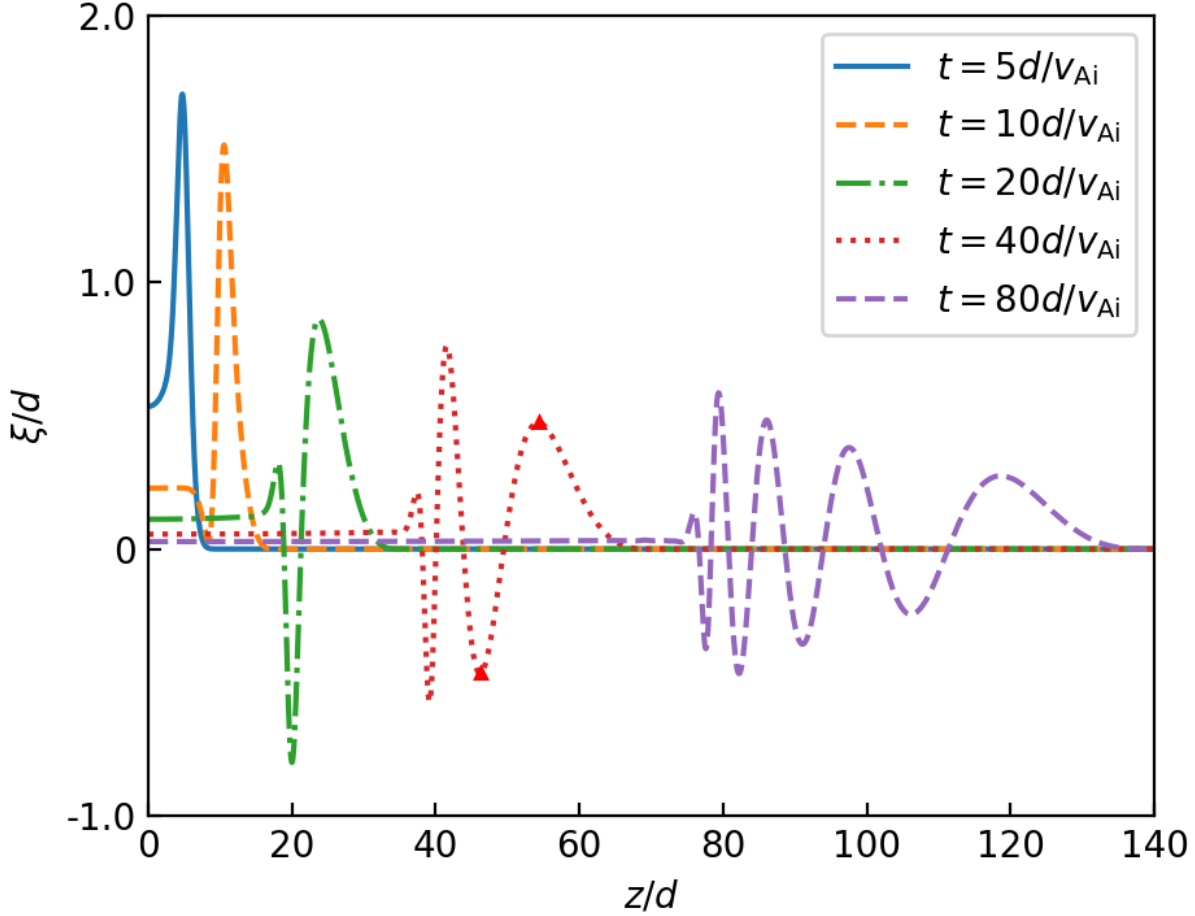


**Figure 2.** The  $z$ -distributions of the transverse displacement  $\xi(x, z, t)$  along the slab axis ( $x = 0$ ) at various instants as labelled. The red triangles mark the outermost crest and trough at  $t = 40d/v_{Ai}$ .

local axial wavenumbers if they are associated with portion  $2^-$ . This expectation, however, is not seen.

We now address question one by showing the  $t - z$  distribution of the transverse displacement  $\xi(x = 0, z; t)$  in Figure 3a. The emergence of crests and troughs is evident, and for simplicity we focus on the solid and dashed curves that thread crest 1 and trough 1, respectively. These local phases at  $t = 40 d/v_{Ai}$  are further highlighted by the red triangles. We take crest 1 as example and demonstrate how to visualize when/where it becomes fully developed by assuming that only portion  $1^-$  is involved. Briefly speaking, plotted in Figure 3a is the numerical output  $\xi(x = 0, z_j; t_i)$  for a uniform time sequence  $\{t_i\}$  and a uniform grid  $\{z_j\}$ . The location  $h_i$  and its temporal derivative  $(dh/dt)_i$  can be found for crest 1 at an arbitrary  $t_i$ . By construction,  $(dh/dt)_i$  and  $h_i/t_i$  represent the local phase and group speeds at  $t_i$ , and the values of  $k_i$  as determined from  $v_{ph}(k_{i,ph}) = (dh/dt)_i$  and  $v_{gr}(k_{i,gr}) = h_i/t_i$  should be the same if crest 1 is fully developed (see the discussions in Sect.2.1). The blue and black circles in Figure 3b then plot the  $h_i$ -dependencies of  $\{k_{i,ph}\}$  and  $\{k_{i,gr}\}$ , respectively. Repeating the same procedure further yields the blue and black diamonds that represent  $\{k_{i,ph}\}$  and  $\{k_{i,gr}\}$  for trough 1. For both local phases, one sees that the black circles somehow fluctuate, which we find difficult to quench. Regardless, the circles in differ-

ent colors experience some systematic deviation only below  $\sim 20 d$ , meaning that this is the critical distance for crest 1 to become fully developed. Likewise, one deduces a critical distance of  $\sim 30 d$  for trough 1, despite that it becomes discernible at a distance of  $\sim 10 d$  (see Figure 3a). With this we illustrate that a given phase needs to propagate some time/distance to become fully developed. More importantly, the circles (diamonds) in Figure 3b yield a consistent value of  $k_i d \approx 0.3$  ( $\approx 0.55$ ) for crest 1 (trough 1) at  $t = 40 d/v_{Ai}$  (the red triangles in Figure 3b). This quantifies the increase of the apparent wavelength from trough 1 to crest 1 (see Figure 2). We remark that this quantification is not trivial, because it does not make much sense to do this by counting the number of extrema per unit length.

### 3 LINEAR AND NONLINEAR COMPUTATIONS IN FINITE- $\beta$ MHD

Now we proceed to the computations of a finite  $\beta$  and continuous density distributions. A more realistic equilibrium under the coronal condition is considered. The initial parameters are listed in Table 1. The plasma  $\beta$  is 0.02 inside the slab at initial state. The transverse density profile is chosen as

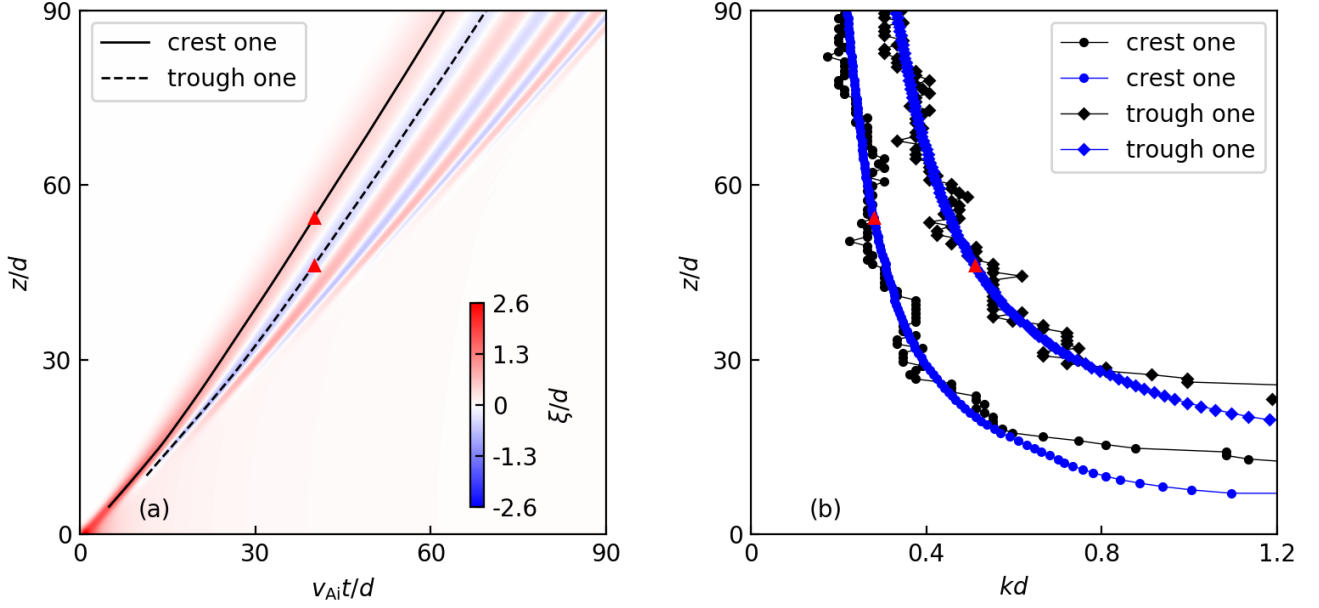


**Figure 3.** Left: Distribution in the  $t - z$  plane of the transverse displacement ( $\xi$ ) along the slab axis ( $x = 0$ ). The outermost crest (trough) is highlighted with the solid (dashed) curve. Right: The local axial wavenumber  $k$  as a function of  $z$  for the outermost crest and trough as determined with the local phase (the black symbols) and group (blue) speeds. The red triangles mark the outermost crest and trough at  $t = 40d/v_{Ai}$ . See text for details.

**Table 1.** Parameters used in finite  $\beta$  simulations. The internal slab density  $\rho_i$  in  $\text{cm}^{-3}$ , internal magnetic field  $B_i$  in G, temperature  $T$  in Kelvin, and the half width  $d$  in Mm.

$\rho_i$	$B_i$	$T$	$\rho_i/\rho_e$	$d$
$3 \times 10^6$	1	$1 \times 10^6$	3	100

$$\rho(x) = \rho_e + (\rho_i - \rho_e)\zeta(x), \quad (8)$$

where

$$\zeta(x) = \frac{1}{1 + (x/d)^\alpha}, \quad (9)$$

where  $\alpha = 10$  gives the steepness of the transverse density profile. The initial density distribution has been presented in the leftmost column of Figure 4. The temperature  $T$  is uniform throughout the computational domain. To maintain magnetostatic pressure balance, the magnetic field  $\mathbf{B} = B(x)\hat{z}$  has a slight variation from the internal region of the slab to the external medium.

We employ the same initial perturbation as given by Equation (4). In the following computations, the magnitude of the initial velocity  $v_0$  is chosen to be  $0.1v_{Ai}$  and  $3v_{Ai}$  in two different runs to distinguish between linear and non-linear regimes.

### 3.1 Numerical Setup

We use the PLUTO code (Mignone et al. 2007) to solve the ideal MHD equations. The HLLD Riemann solver is used to compute the numerical fluxes. We use the piecewise parabolic method for spatial reconstruction and the second-order Runge-Kutta algorithm for time marching. The hyperbolic divergence cleaning method is adopted to maintain the divergence-free condition of the magnetic field. The two-dimensional computational domain is  $[-100, 100]d \times [-300, 300]d$ , making sure that the boundaries are sufficiently far

such that no reflections would influence the concerned region. We consider a uniform mesh of 1000 points in the  $x$ -direction and 3000 uniformly spaced cells in the  $z$ -direction. A convergence study with more grid cells shows no significant influence on the current results.

The boundary conditions are specified as follows. We fix the transverse velocities at both ends of the slab to be zero, while  $v_z$ ,  $B_x$  are set to have zero-gradients. Since the ends of the slab are sufficiently far from the initial perturbation, the boundary set in the  $z$ -direction does not influence the concerned domain. The other variables are fixed to the initial value. In addition, we adopt outflow conditions to be the lateral boundaries in the  $x$ -direction.

### 3.2 Numerical Results

We conduct a preliminary examination of the dynamics of the magnetic slab with the help of density evolution maps. Figure 4 displays density snapshots for both linear (the upper row) and nonlinear (lower) runs at the initial state and later instants. Fast waves propagation can be observed in both runs, as shown by the velocity fields in Figure 4. However, no obvious density perturbations can be observed in the linear regime (the upper row of Figure 4). In Figures 4b2 and 4b3, however, the density structure has noticeable displacements. Kink waves characterized by transverse displacements of the slab axis can also be observed in Figure 4b2 and Figure 4b3. Besides this, one can find two other apparent signatures: the occurrence of a density cavity inside the slab near the exciter (clearly seen in Figure 4b3) and the propagation of density disturbances outside the slab.

We first focus on the nonlinearity-induced signatures before proceeding to the analysis of the excited kink wave trains. Figure 5a presents the density variations ( $\Delta\rho = \rho(t) - \rho_0$ ) relative to the initial state at  $t = 8.19d/v_{Ai}$ . Only the upper half of the concerned region is presented in view of the relevant symmetry. One sees a density cavity characterized by some blue area inside the slab ( $-d < x < d$ ) from  $z = 0$  to nearly  $z = 3d$ . Some density enhancement surrounding the cavity can also be seen. The  $z$ -component of the pressure gra-

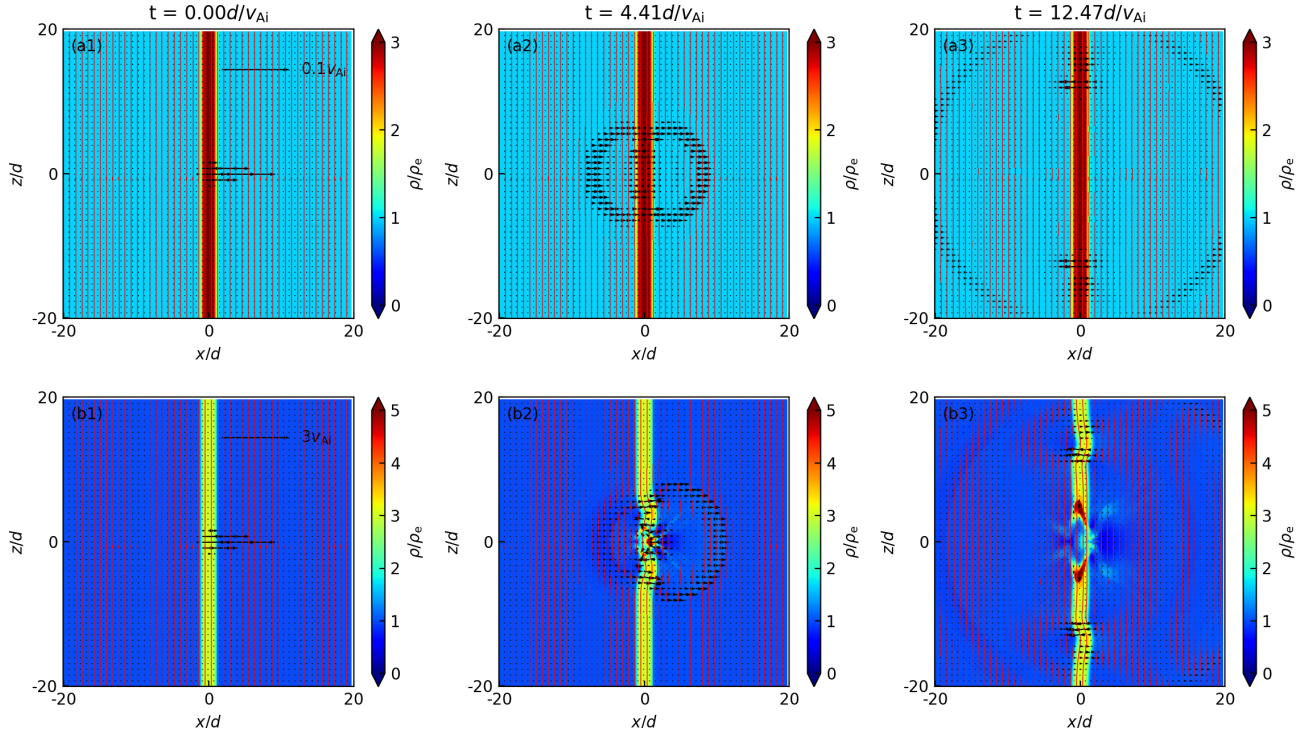


**Figure 4.** Evolution of normalized density distribution for linear (the upper row) and nonlinear (lower) computations at different instants as labeled. Magnetic lines of force (the red curves) and velocity fields (the black arrows) are overlotted.

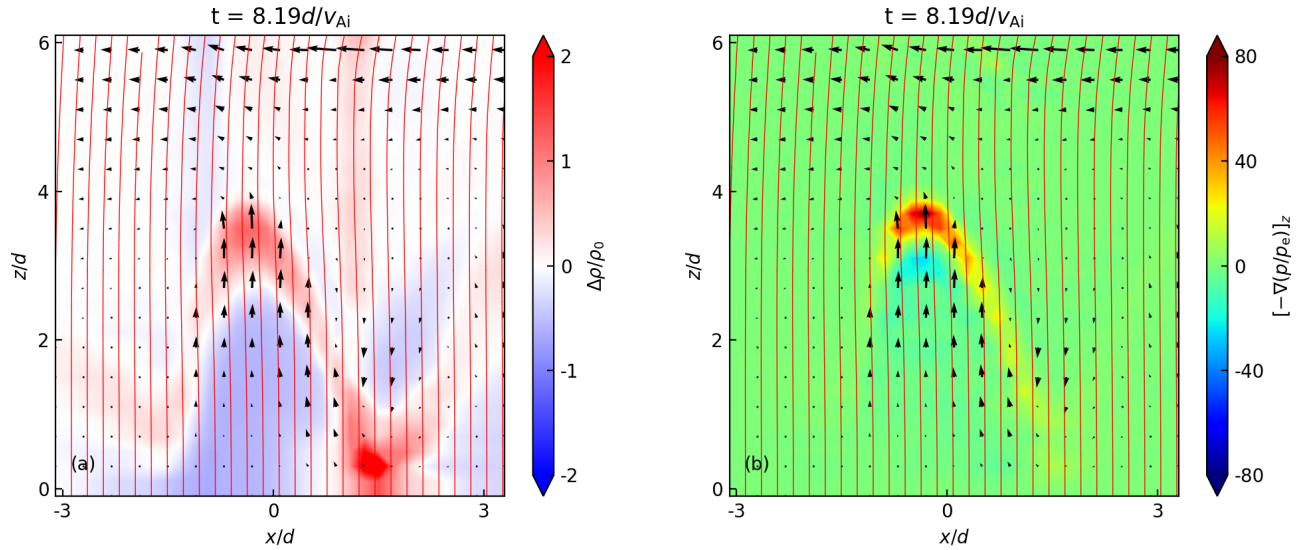


**Figure 5.** Left: Distribution of the density variation ( $\Delta\rho = \rho(t) - \rho_0$ ) relative to the initial state  $\rho_0$  at  $t = 8.19d/v_{Ai}$ . Right: Plots of the  $z$ -component of pressure gradients in the same region as in the left panel at  $t = 8.19d/v_{Ai}$ . The pressure is normalized by the external value  $p_e$ . Magnetic field lines (red) and velocity fields (black) are also overlotted in each panel.

gradient defined by  $[-\nabla(p/p_e)]_z$  has been plotted in Figure 5b. One sees large pressure gradients accompanied by upward velocities in the dense area. This means that the nonlinear initial pulse causes an increase in the local pressure gradient, thereby inducing an upward flow and redistributing the local density. A similar scenario has also been discussed by Terradas & Ofman (2004) in the reaction of a coronal loop to transverse perturbations. In that case, a flow is also

induced by the ponderomotive force, causing the expansion of the loop.

Another noteworthy signature in the nonlinear computation is the propagation of fast waves characterized by density enhancements. As shown in Figure 4b2, a wavefront indicated by the density enhancement moves outside the slab. The wavefront is much clearer in the  $x > 0$  region since the initial perturbation is directed along the positive  $x$ -axis. Figure 6 shows the distribution of the velocity

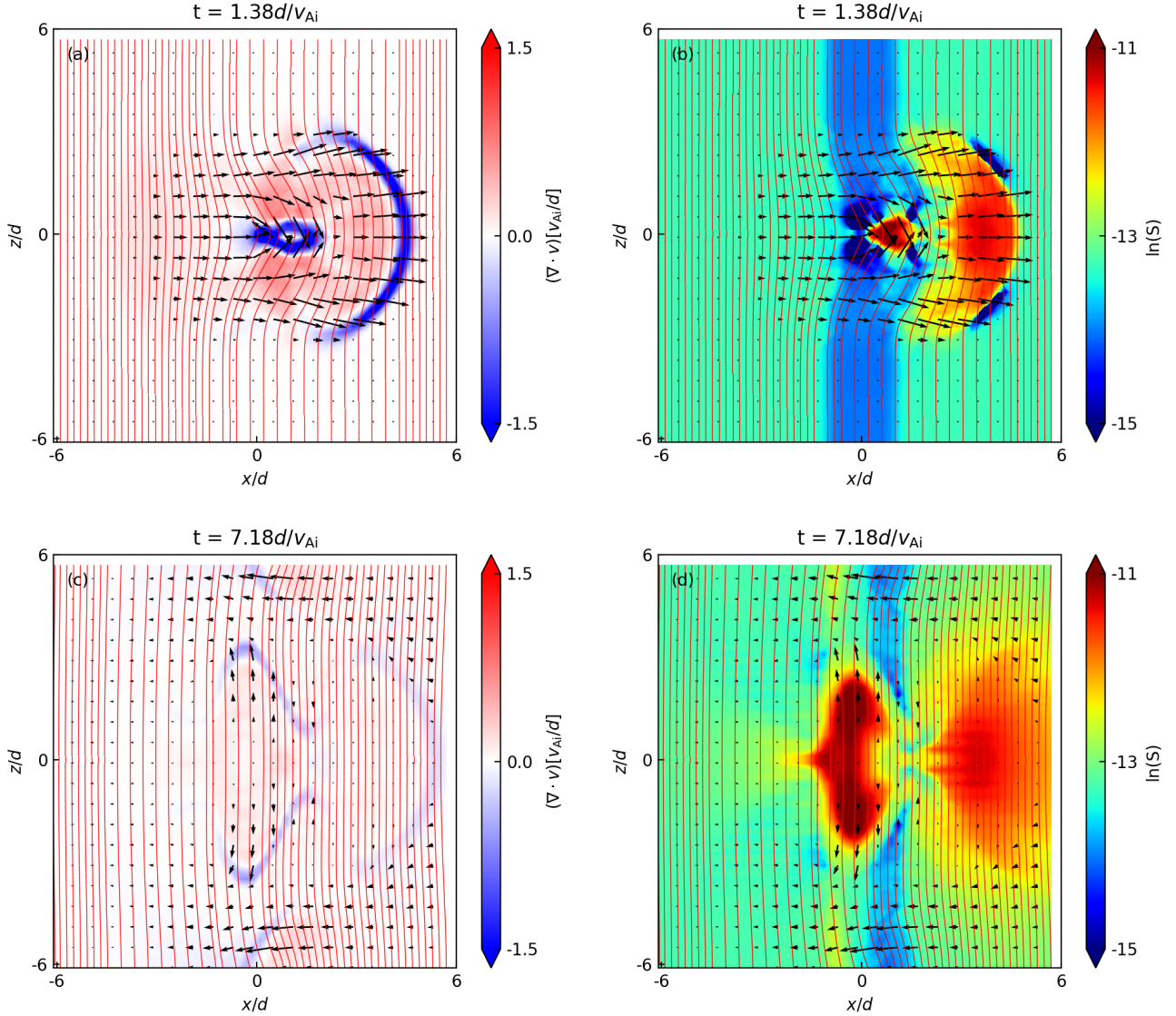


**Figure 6.** Snapshots of the velocity divergence ( $\nabla \cdot \mathbf{v}$ ) and the entropy ( $S = p\rho^{-\gamma}$ ) at different times as labelled. Magnetic field lines (red) and velocity fields (black) are also overplotted in each panel.

divergence ( $\nabla \cdot \mathbf{v}$ ) and the logarithmic entropy ( $\ln S$ ) at two different instants as labeled. Here a variable  $S = p\rho^{-\gamma}$  is introduced to measure the specific entropy with  $\gamma = 5/3$  being the adiabatic index. One sees that a wavefront disturbs the magnetic field lines in Figure 6a,b, introducing discontinuous variations in velocity divergence and entropy. This shows the presence of a shock. The downstream magnetic field is refracted away from the shock normal, showing a fast shock property. At a later time, one can also find a wavefront inside the slab in Figure 6c,d. The velocity is directed almost along the magnetic field lines, and the downstream magnetic field is refracted towards the wavefront normal, showing a possible sign of a slow shock. However, this signature is mixed with the upflow shown in Figure 5b. To recognize the slow shock, it is needed to trace their evolution at given positions. Figure 7a,c present the temporal evolution of velocity divergence and entropy at  $x = 0$  and  $y = 0$ . One sees the fast shock front characterized by a negative velocity divergence (blue stripes) in the region I of Figure 7a, followed by rarefactions characterized by a bundle of red stripes. The discontinuity of the

entropy in Figure 7c proves again that the outside propagating disturbances steepen into shocks. The propagation speed of the shock front measured from Figure 7c is larger than the local fast speed. This confirms again a fast shock. Region II in Figure 7 reveals a fast wave reflected by the slab lateral boundaries. In addition, one can now find the slow shock hidden by the pressure-induced flow inside the slab. A similar distribution of red and blue stripes can also be found in region II of Figure 7b, manifesting a shock wave moving along the slab. Due to the pressure-induced flow, however, the shock front can only be recognized after about  $t = 17d/v_{Ai}$  in Figure 7d. Again, the propagation speed of the shock front measured from Figure 7d is larger than the local sound speed but much smaller than the local Alfvén speed. This confirms a slow shock. Seen from Figure 7c, the density cavity shows no oscillatory property, but shrink to  $x = 0$  after  $\sim 4v_{Ai}/d$ . Note that the enhancements of entropy in about  $z < 4d$  in Figure 7d are induced by the density cavity. The trajectory of a given parcel ( $[tv_{Ai}/d, z/d] = [10.08, 3.01]$ ) is traced, shown by the white

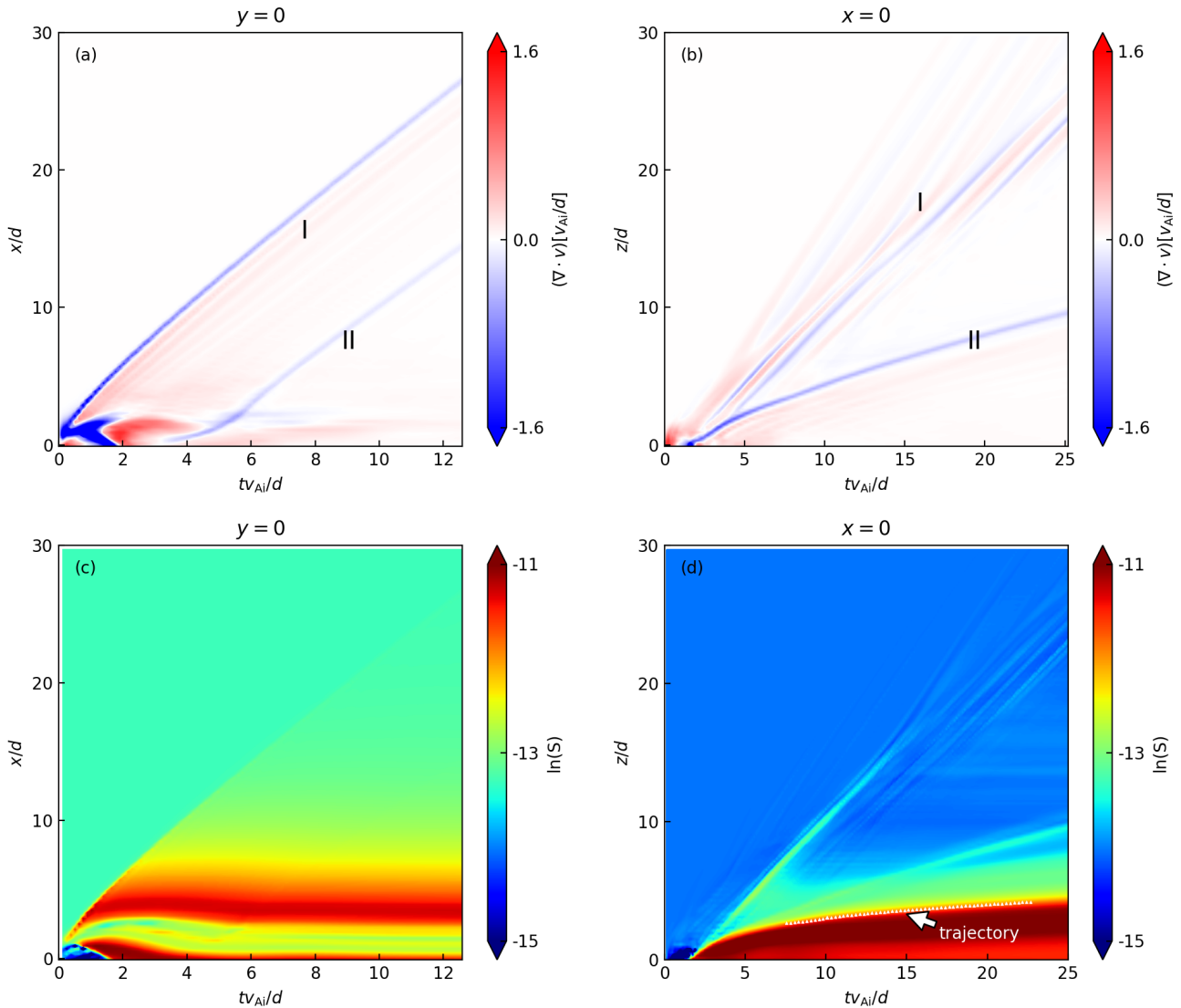


**Figure 7.** Upper: Time-distance map of the velocity divergence  $(\nabla \cdot \mathbf{v})$  at (a)  $y = 0$  and (b)  $x = 0$ . Lower: Time-distance map of the entropy  $S = p\rho^{-\gamma}$  at (c)  $y = 0$  and (d)  $x = 0$ . Pressure  $p$  and density  $\rho$  are numerically dimensionless. White symbols in the lower panel represents the parcel trajectory of a given point  $[tv_{Ai}/d, z/d] = [10.08, 3.01]$ . See text for details.

symbols in Figure 7d<sup>2</sup>. The parcel trajectory coincides with the boundary of the density cavity, meaning that the cavity is associated with plasma flows rather than being a genuine wave. The red and blue stripes in the region I in Figure 7b are a signal of fast wave trains in the slab, manifesting the compressibility of kink waves. Similar slow shocks can also be observed when perturbing a slab with symmetric initial perturbations, as discussed by Pascoe et al. (2017).

Now we examine the properties of the excited kink wave trains in the slab with a finite plasma  $\beta$ . Similar to Figure 2, we present transverse velocity  $v_x$  for both linear and nonlinear regimes at different times in Figure 8<sup>3</sup>. The transverse velocity is normalized by the

<sup>2</sup> This parcel trajectory is the projection of the trajectory in the  $[x, z]$  space on the  $z$ -direction. It is very close to the real one since the  $v_x$  is nearly zero in the time interval we considered.

<sup>3</sup> One may find that the profiles in Figure 8 differ from those in Figure 2, especially in the initial stage. The reason is that different instants are chosen in these two figures.

initial velocity amplitude  $v_0$  for both cases. One sees that the wave properties of the two regimes are similar at given instants, showing no significant influence of the amplitude of initial perturbations on the wave profiles, despite the density variations and shocks in the nonlinear computation. Meanwhile, the properties that more oscillatory patterns emerge with time and wavelength increases at a given time show up as happens in the  $\beta = 0$  calculation in Figure 2. The understanding of these properties has been illustrated in Section 2. Note that the wave profiles show no steepening as time evolves. The reasons are twofold. First, the wave energy distributes to larger areas as time proceeds, leading to a decrease in the velocity amplitude. Second, as demonstrated in previous sections, the head of the wave train moves faster than its tail, thus no steepening can be observed. We note that the continuous density distribution and the occurrence of fast/slow shocks do not influence the oscillatory properties of fast kink wave trains in the slab.

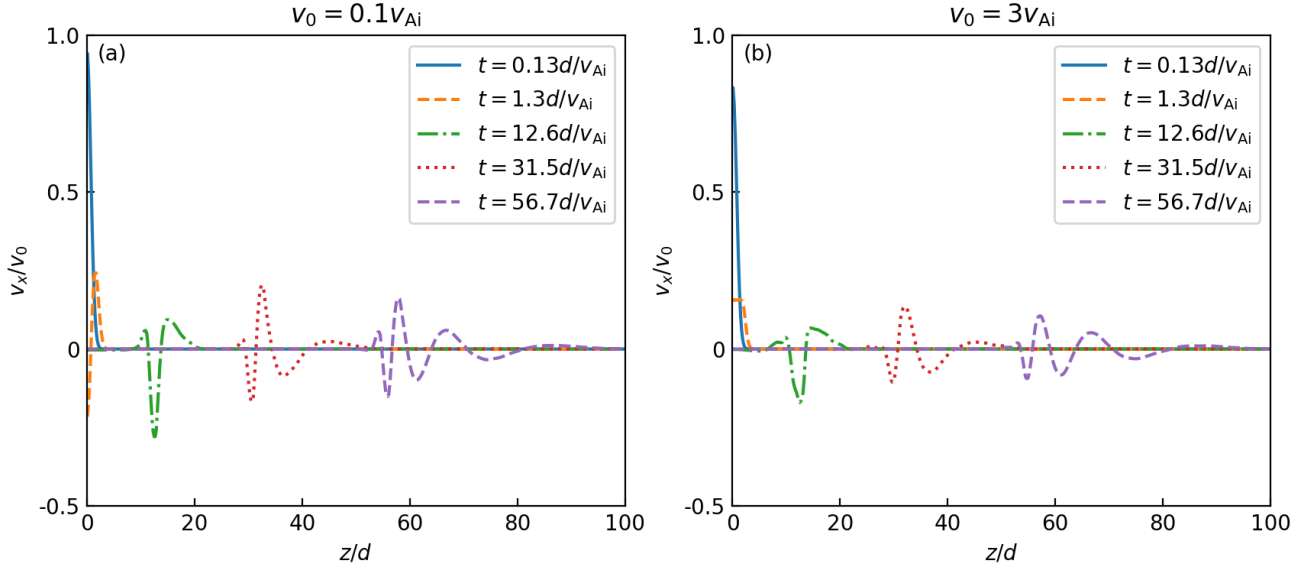


**Figure 8.** The  $z$ -distributions of the normalized transverse velocity  $v_x/v_0$  along the slab axis ( $x = 0$ ) at various instants as labelled. The time  $t$  is measured in units of  $d/v_{Ai}$ .

#### 4 POTENTIAL APPLICATION TO STREAMER WAVES

Kink wave trains in slabs are intuitively related to streamer wave observations. Actually, three signatures have been reported in imaging observations of streamer waves (e.g., [Chen et al. 2010](#); [Kwon et al. 2013](#)). Signature 1, more oscillatory patterns emerge as time progresses. Signature 2, the apparent wavelength increases with distance at a given time. Both signatures were evident in the sequence of LASCO C2 and C3 running difference images ([Chen et al. 2010](#), Figure 4). Signature 3, the cyclic motion tends to be rapidly attenuated at small heliocentric distances, evidenced in the STEREO/COR1 measurements (see [Kwon et al. 2013](#); Figures 5 and 6). Our numerical results have shown that Signatures 1 and 2 are compatible with a simple picture where streamer waves are impulsively excited kink wave trains in density-enhanced stalks even when the propagation is strictly two-dimensional and when the equilibrium is axially uniform, regardless of the reality of a finite plasma  $\beta$  and nonlinear effects.

Our nonlinear calculation seems not appropriate to reproduce the observational properties of Signature 3 close to the exciter. Due to the occurrence of the density cavity, it would be not easy to recognize a magnetic slab structure there, thus Signature 3 cannot be discussed. However, the observational events associated with Signature 3, such as the streamer waves reported by [Kwon et al. \(2013\)](#), are excited by external pulses (e.g., CMEs) at streamer helmet bases. Therefore the density cavity can not be observed in the streamer stalks. However, if a CME impinges on a streamer stalk from the side, the appearance of a density cavity would be possible. In this case, however, detections of such a density cavity would still be a challenge. Firstly, the intensity of the density cavity is determined by the magnitude of perturbations and interaction time between CMEs and streamer stalks. Therefore high spatial and temporal resolutions of instruments are necessary. Secondly, the intensity distribution of streamer stalks tends to be diffuse, and the density contrast between streamer stalks and background corona is not large enough (see Figure 2 in [Chen et al. 2011](#)). This observational fact may also introduce difficulties in recognizing a density cavity in a streamer stalk. In addition, CMEs probably do not impinge on the stalks perpendicularly, and the potential flow may

fall back due to gravity. These possibilities also influence convincing detections of a density cavity in streamer stalks.

#### 5 CONCLUSIONS

In this paper we examined the reaction of coronal slabs to both linear and nonlinear localized transverse velocity perturbations, considering both plasma  $\beta = 0$  and a finite plasma  $\beta$  effect. All computations confirm the presence of fast kink wave trains in the slab. The wave trains present the emergence of more oscillatory patterns with time and the apparent increase of wavelength with distance at a given instant, regardless of the nonlinearity and the reality of a finite plasma  $\beta$ . Particularly, a density cavity and enhancement near the exciter are observed in the nonlinear computation. In addition, fast/slow shocks are also obtained in the nonlinear regime.

Potential applications of the current results of kink wave trains in coronal slabs are related to the typical observations of streamer waves. All the computations can reproduce the observational signatures of streamer waves that more oscillatory patterns emerge as time marches and the apparent wavelength increases with distance at a given time. Our linear calculations can also reproduce the rapid damping of streamer waves at small heliocentric distances, regardless of the reality of a finite plasma  $\beta$  and density distributions. The nonlinear calculations with a finite  $\beta$  consideration predict the occurrence of a density cavity in streamer stalks when the fierce activities, such as CMEs interact directly with streamer stalks rather than the streamer helmet bases.

#### ACKNOWLEDGEMENTS

We gratefully acknowledge ISSI-BJ for supporting the international team "Magnetohydrodynamic wavetrains as a tool for probing the solar corona". This work was supported by the National Natural Science Foundation of China (41974200, 11761141002, 41904150) and the European Research Council (ERC) under the European Union's

Horizon 2020 research and innovation programme (grant agreement No.724326).

## DATA AVAILABILITY

The data underlying this article are available in the article and in its references.

## REFERENCES

- Anfinogentov S., Nisticò G., Nakariakov V. M., 2013, *A&A*, **560**, A107
- Arregui I., 2015, *Philosophical Transactions of the Royal Society of London Series A*, **373**, 20140261
- Aschwanden M. J., Fletcher L., Schrijver C. J., Alexander D., 1999, *ApJ*, **520**, 880
- Chen Y., Song H. Q., Li B., Xia L. D., Wu Z., Fu H., Li X., 2010, *ApJ*, **714**, 644
- Chen Y., Feng S. W., Li B., Song H. Q., Xia L. D., Kong X. L., Li X., 2011, *ApJ*, **728**, 147
- De Moortel I., Nakariakov V. M., 2012, *Philosophical Transactions of the Royal Society of London Series A*, **370**, 3193
- Decraemer B., Zhukov A. N., Van Doorselaere T., 2020, *ApJ*, **893**, 78
- Edwin P. M., Roberts B., 1982, *Sol. Phys.*, **76**, 239
- Edwin P. M., Roberts B., 1983, *Sol. Phys.*, **88**, 179
- Edwin P. M., Roberts B., 1986, in NASA Conference Publication. pp 347–357
- Feng S. W., Chen Y., Li B., Song H. Q., Kong X. L., Xia L. D., Feng X. S., 2011, *Sol. Phys.*, **272**, 119
- Gao Y., Li F., Li B., Cao W., Song Y., Tian H., Guo M., 2021, *Sol. Phys.*, **296**, 184
- Guo M.-Z., Chen S.-X., Li B., Xia L.-D., Yu H., 2016, *Sol. Phys.*, **291**, 877
- Guo M., Van Doorselaere T., Karpelas K., Li B., Antolin P., De Moortel I., 2019, *ApJ*, **870**, 55
- Howson T. A., De Moortel I., Antolin P., 2017, *A&A*, **602**, A74
- Jess D. B., Mathioudakis M., Erdélyi R., Crockett P. J., Keenan F. P., Christian D. J., 2009, *Science*, **323**, 1582
- Karpelas K., Van Doorselaere T., Antolin P., 2017, *A&A*, **604**, A130
- Kohutova P., Verwichte E., Froment C., 2020, *A&A*, **633**, L6
- Kolotkov D. Y., Nakariakov V. M., Moss G., Shellard P., 2021, *MNRAS*, **505**, 3505
- Kwon R.-Y., Ofman L., Olmedo O., Kramar M., Davila J. M., Thompson B. J., Cho K.-S., 2013, *ApJ*, **766**, 55
- Li B., Guo M.-Z., Yu H., Chen S.-X., 2018, *ApJ*, **855**, 53
- Li B., Antolin P., Guo M. Z., Kuznetsov A. A., Pascoe D. J., Van Doorselaere T., Vasheghani Farahani S., 2020, *Space Sci. Rev.*, **216**, 136
- Li B., Chen S.-X., Li A.-L., 2022, *ApJ*, **928**, 33
- Liu W., Ofman L., 2014, *Sol. Phys.*, **289**, 3233
- Liu W., Title A. M., Zhao J., Ofman L., Schrijver C. J., Aschwanden M. J., De Pontieu B., Tarbell T. D., 2011, *ApJ*, **736**, L13
- Lopin I., Nagorny I., 2015, *ApJ*, **801**, 23
- Magyar N., Nakariakov V. M., 2020, *ApJ*, **894**, L23
- Mignone A., Bodo G., Massaglia S., Matsakos T., Tesileanu O., Zanni C., Ferrari A., 2007, *ApJS*, **170**, 228
- Morton R. J., Verth G., Jess D. B., Kuridze D., Ruderman M. S., Mathioudakis M., Erdélyi R., 2012, *Nature Communications*, **3**, 1315
- Murawski K., Roberts B., 1993a, *Sol. Phys.*, **144**, 101
- Murawski K., Roberts B., 1993b, *Sol. Phys.*, **145**, 65
- Nakariakov V. M., Kolotkov D. Y., 2020, *ARA&A*, **58**, 441
- Nakariakov V. M., Ofman L., 2001, *A&A*, **372**, L53
- Nakariakov V. M., Ofman L., Deluca E. E., Roberts B., Davila J. M., 1999, *Science*, **285**, 862
- Nakariakov V. M., Arber T. D., Ault C. E., Katsiyannis A. C., Williams D. R., Keenan F. P., 2004, *MNRAS*, **349**, 705
- Nakariakov V. M., et al., 2021, *Space Sci. Rev.*, **217**, 73
- Oliver R., Ruderman M. S., Terradas J., 2014, *ApJ*, **789**, 48
- Oliver R., Ruderman M. S., Terradas J., 2015, *ApJ*, **806**, 56
- Pascoe D. J., Nakariakov V. M., Kupriyanova E. G., 2013, *A&A*, **560**, A97
- Pascoe D. J., Nakariakov V. M., Kupriyanova E. G., 2014, *A&A*, **568**, A20
- Pascoe D. J., Goddard C. R., Nakariakov V. M., 2017, *ApJ*, **847**, L21
- Roberts B., Edwin P. M., Benz A. O., 1983, *Nature*, **305**, 688
- Roberts B., Edwin P. M., Benz A. O., 1984, *ApJ*, **279**, 857
- Rosenberg H., 1970, *A&A*, **9**, 159
- Shi M., Van Doorselaere T., Guo M., Karpelas K., Li B., Antolin P., 2021, *ApJ*, **908**, 233
- Spruit H. C., 1982, *Sol. Phys.*, **75**, 3
- Terradas J., Ofman L., 2004, *ApJ*, **610**, 523
- Terradas J., Oliver R., Ballester J. L., 2005, *A&A*, **441**, 371
- Tian H., McIntosh S. W., Wang T., Ofman L., De Pontieu B., Innes D. E., Peter H., 2012, *ApJ*, **759**, 144
- Tian H., Young P. R., Reeves K. K., Wang T., Antolin P., Chen B., He J., 2016, *ApJ*, **823**, L16
- Van Doorselaere T., Brady C. S., Verwichte E., Nakariakov V. M., 2008, *A&A*, **491**, L9
- Van Doorselaere T., et al., 2020, *Space Sci. Rev.*, **216**, 140
- Verwichte E., Nakariakov V. M., Cooper F. C., 2005, *A&A*, **430**, L65
- Wang T., Ofman L., Davila J. M., Su Y., 2012, *ApJ*, **751**, L27
- Wentzel D. G., 1979, *A&A*, **76**, 20
- Whitham G., 1974, *Linear and Nonlinear Waves* John Wiley & Sons
- Williams D. R., et al., 2001, *MNRAS*, **326**, 428
- Yu H., Li B., Chen S.-X., Xiong M., Guo M.-Z., 2016, *ApJ*, **833**, 51
- Yu H., Li B., Chen S.-X., Xiong M., Guo M.-Z., 2017, *ApJ*, **836**, 1
- Yu H., Li B., Chen S., Guo M., 2021, *Sol. Phys.*, **296**, 95
- Zaitsev V. V., Stepanov A. V., 1982, *Soviet Astronomy Letters*, **8**, 132
- Zaitsev V. V., Stepanov A. V., 1975, *Issledovaniia Geomagnetizmu Aeronomii i Fizike Solntsa*, **37**, 3
- Zimovets I. V., et al., 2021, *Space Sci. Rev.*, **217**, 66

This paper has been typeset from a  $\text{\TeX}/\text{\LaTeX}$  file prepared by the author.